Adhesion and Atomic Structures of Gold on Ceria Nanostructures: The Role of Surface Structure and Oxidation State of Ceria Supports

Yuyuan Lin,[†,] Zili Wu,[‡,*] Jianguo Wen,[§] Kunlun Ding,[∥] Xiaoyun Yang,[⊿] Kenneth R. Poeppelmeier,[∥] and Laurence D. Marks[†,*]*

[†]Department of Materials Science and Engineering, Northwestern University, Evanston, Illinois, 60208, USA

[‡]Chemical Science Division and Center for Nanophase Materials Sciences, Oak Ridge National Laboratory, Oak Ridge, Tennessee, 37831, USA

[§]Electron Microscopy Center, Argonne National Laboratory, Argonne, Illinois 60439, USA

[⊿]2112 Vincenzo Walkway, San Jose, California, 95133, USA

[∥]Department of Chemistry, Northwestern University, Evanston, Illinois 60208, USA

TABLE OF CONTENTS GRAPHIC

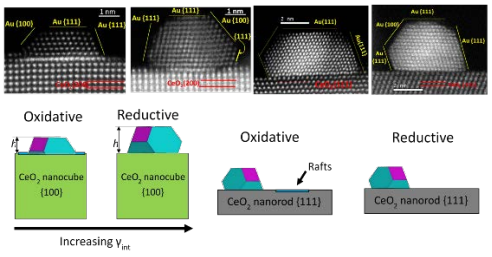

ABSTRACT: We report an aberration-corrected electron microscopy analysis of the adhesion and atomic structures of gold nanoparticle catalysts supported on ceria nanocubes and nanorods.

Under oxidative conditions, the as-prepared gold nanoparticles on the ceria nanocubes have extended atom layers at the metal-support interface. In contrast, regular gold nanoparticles and rafts are present on the ceria nanorod supports. Under the reducing conditions of water-gas shift reaction, the extended gold atom layers and rafts vanish. In addition, the gold particles on the nanocubes change in morphology and increase in size while those on the nanorods are almost unchanged. The size, morphology, and atomic interface structures of gold strongly depend on the surface structures of ceria supports ((100) surface versus (111) surface) and the reaction environment (reductive versus oxidative). These findings provide mechanistic insights into the deactivation mechanisms and the shape-dependent catalysis of oxide supported metal catalysts.

KEYWORDS: gold, ceria, atomic structures, adhesion, aberration corrected STEM HAADF, nanocube, nanorods, catalysis

It is well-known that supported metal nanoparticle catalysts must be considered as a composite of the support and metal. This is known as the metal-support interactions. Different cases occur such as different epitaxies of the metal depending upon the support surface terminations,[1, 2] strong metal-support interactions (SMSI),[3-6] and sites at the metal-support interface.[7] The SMSI includes both geometric and electronic effects between the metal and support.[8-12] It is clear that the oxide can act more than just a passive template for nanoparticle epitaxy. There was recent work where metal-support interface has been combined with shape-controlled nanostructures.[13, 14] We show here one case at atomic resolution for the gold-ceria (Au-CeO_2) system, that both the oxidation states and the atomic surface structures of ceria play a significant role in the adhesion of Au.

The Au-CeO_2 system is an excellent model system for investigating the effect of oxidation state on the metal-support interface: (1) the morphology and surface structures of Au nanoparticles have been investigated extensively.[15] (2) The exposed facet of CeO_2 nanostructures can be controlled[13, 16] and the atomic surface structures of CeO_2 nanoparticles have been determined.[17] (3) The Au-CeO_2 system has attracted great interest in heterogeneous catalysis.[18-21] The bulk form of Au is typically inert,[22] while supported Au nanoparticles have been shown to be active for CO oxidation,[23] which has triggered a significant number of further studies on the reaction mechanisms.[24-27] The low coordinate Au atoms,[28] electronic effect,[29] and support effect[30] have all been proposed to explain the enhanced activity of the nanoparticle Au catalysts. The long-recognized redox capabilities of CeO_2 nanoparticles[16] make them one of the most popular oxide supports for Au catalysts.[31-35] In addition, different catalytic behaviors have been observed for Au catalysts supported by CeO_2 nanorods, nanocubes, and other nanostructures.[20, 30, 36-38] The CeO_2 nanorods and nanocubes can have the {111} and {100} facets exposed.[17, 39] Differences in the redox properties of each facet are generally attributed to the distinct catalytic properties. However, clearly how the redox properties impacts the Au-CeO_2 system is still unknown. The different CeO_2 nanostructures can also impact the size, morphology, and interface structures of Au catalysts through the metal-support interaction.[39-43] Furthermore, the Au-CeO_2 catalysts may undergo changes when subjected to reactions such as water-gas shift (WGS), which puts the catalyst under a different atmosphere (reductive) from that used for the catalyst pretreatment (oxidative). To the best of our knowledge, a systematic comparative study on the adhesion and atomic structures of the Au-CeO_2 system subjected to these conditions has not been reported. In this study we have performed aberration-corrected high angle annular dark field (HAADF) scanning transmission electron microscopy (STEM)

imaging on Au-CeO_2 nanostructures with well-defined shapes. With atoms clearly resolved, the size, morphology, and atomic interface structures of the Au-CeO_2 catalysts before and after the WGS reaction are systematically analyzed.

The CeO_2 nanocubes and nanorods were prepared using a previously reported method.[44] In a typical synthesis, 0.868 g of $Ce(NO_3)_3 \cdot 6H_2O$ and 9.6 g of NaOH were dissolved in 5 and 35 ml of deionized water. The two solutions were mixed and transferred to a 125 ml autoclave with a Teflon liner. The autoclave was then heated to 373 and 453 K for 24 h to obtain nanorods and nanocubes, respectively. The as-collected nanostructures were washed and dried at 90 ºC overnight. In addition, the CeO_2 nanorods were annealed at 700 ºC for 2 hours in air in order to reduce the number of surface defects.[39] The surface areas of the obtained ceria nanocubes and nanorods were determined to be 25 and 59 m^2/g, respectively. Au nanoparticles were deposited on the CeO_2 nanostructures using a deposition-precipitation method similar to that used by Zanella et al.[45] For both CeO_2 nanorods and nanocubes, 0.5 g CeO_2, 55 mg $HAuCl_3$, 1.28 g urea, and 60 ml H_2O were mixed together to form a suspension. The suspension was stirred and kept at 80 ºC in an oil bath for ~20 h. The end product was washed, collected, and annealed in air at 300 ºC for 3 h. The obtained Au-CeO_2 nanocubes and Au-CeO_2 nanorods were used for the WGS reaction.

The WGS reaction was carried out in an automated reaction system (AMI-200). About 31.2 mg sample was loaded into a U-shaped reactor and treated under helium at 300 ºC for 1 hour before cooling down to room temperature. The sample was then exposed to the WGS reactant mixture: 1% CO/He (5mL) bubbling through a water saturator kept at 22 ºC to give a CO/H_2O ratio of 0.4 (space velocity: 9615 $mL/g_{cat}.h$). The sample was heated (ramp rate 10 ºC/min) to 290 ºC and kept there for a stability test for at least 40 hours. The reactants and products were

continuously analyzed with an online mass spectrometer (OmniStar GSD-301 O2, Pfeiffer Vacuum). All gases were provided by Air Liquide and were UHP grade.

Ex-situ HAADF characterization was performed on the catalysts both before and after the WGS reaction. The HAADF study was conducted using the JEOL ARM 200 STEM at the University of Illinois at Chicago with a probe side spherical aberration corrector operated at 200 KeV.[46] Before a typical HAADF experiment, the Au-CeO_2 nanostructures were mixed with ethanol to make a suspension, and a small amount of the suspension was then applied to a copper grid coated with lacey carbon film. The grid was then transferred into the microscope column with a vacuum of ~10^{-8} Torr. During HAADF characterization, a relative small probe current (~5 μA) with a size of ~0.8 Å was used to balance the signal-to-noise ratio and beam damage. For atomic resolution imaging, the samples were tilted to [100] and [110] zone axes for the CeO_2 nanocubes and nanorods, respectively.

Figure 1a shows a low magnification HAADF image of the as-prepared Au-CeO_2 nanorods. Figure 1b,c show atomic resolution HAADF images of the typical Au-CeO_2 nanorods. The CeO_2 nanorods were tilted to the $[1\bar{1}0]$ zone axis. In the HAADF images, which are often referred to as Z-contrast images, the white spots can be directly interpreted as atom columns. As a result, it is clear that the growth direction of the nanorod is along <112>, and the predominantly exposed facets of the nanorods are {111}. Several different adsorbed Au species can be identified. Regions I and II in Figure 1b are the Au species in the form of "rafts", as they exhibit different interatomic spacing and contrast compared to the CeO_2 support. Figure 1c shows the Au atoms are in the particle form. The interface relationship is Au(111) $[\bar{1}10]$// CeO_2(111) $[\bar{1}10]$. Regions I, II in Figure 1b and the Au particles are all grown on the {111} facets of the nanorod. Only a small portion of the Au is found on the {100} surface (labeled as region III in Figure 1b), which

is a truncated edge of the nanorod. As the (111) surface of CeO_2 nanoparticles is O-terminated,[17] the schematic view of the as-prepared Au-CeO_2 nanorods is show in Figure 1g.

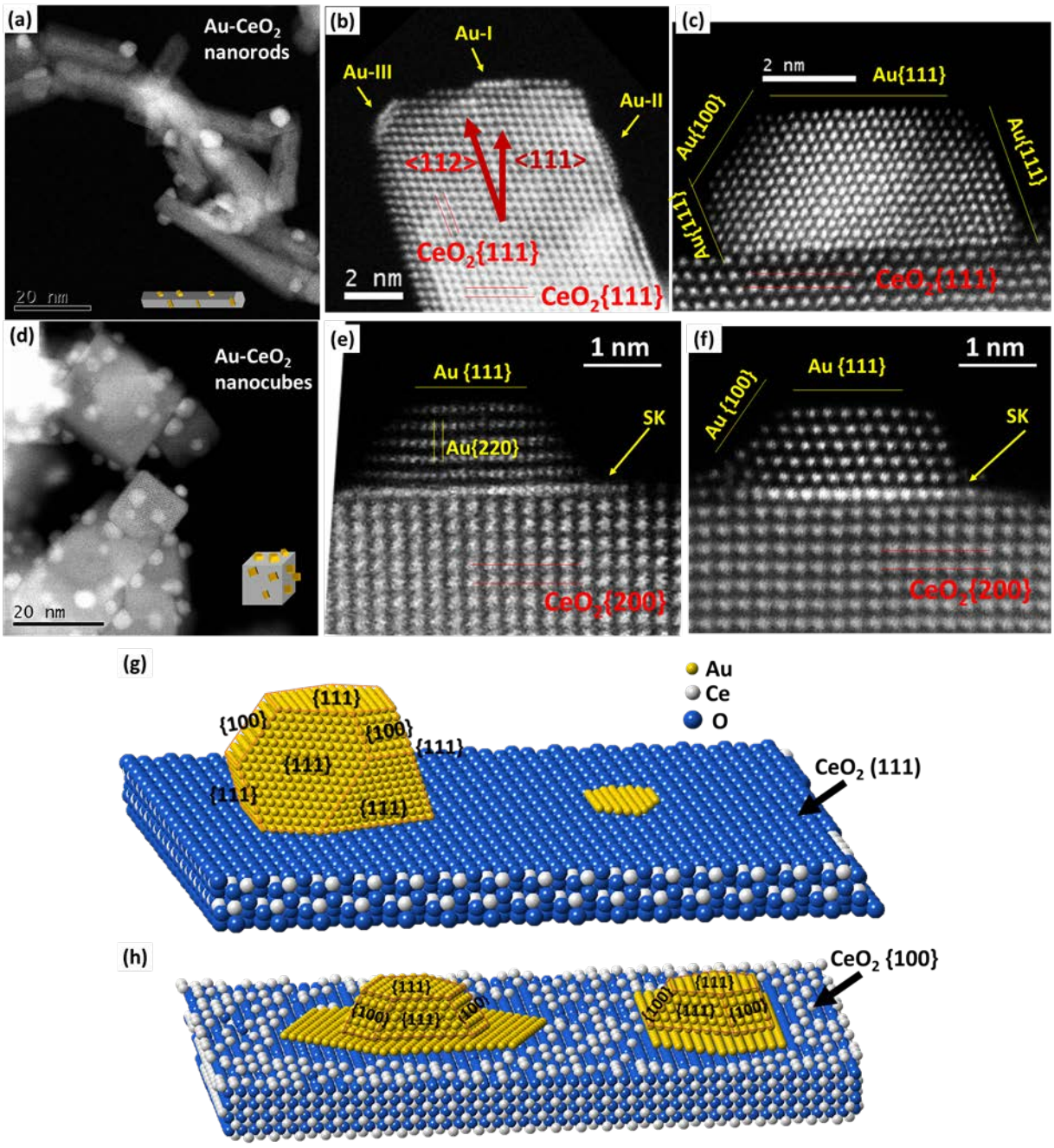

Figure 1. The morphology and atomic structures of Au-CeO_2 nanostructures before the WGS reaction (a) Low magnification HAADF image of Au-CeO_2 nanorods. (b) Atomic resolution HAADF image of Au rafts on a CeO_2 nanorod. (c) Atomic resolution HAADF image of an Au nanoparticle on a CeO_2 nanorod. (d) Low magnification HAADF image of Au-CeO_2 nanocubes. (e) Atomic resolution HAADF image of an Au particle with a Stranski–Krastanov (SK) layer supported by a CeO_2 nanocube. (f) Atomic resolution HAADF image of another Au particle with a SK layer supported by a CeO_2 nanocube. (g) Schematic view of an Au particle and raft supported by the CeO_2 (111) surface. (h) Schematic view of Au particles supported by the CeO_2 (100) surface.

Figure 1d shows a low magnification HAADF image of the as-prepared Au-CeO_2 nanocubes, while Figures 1e,f show atomic resolution HAADF images of the typical Au-CeO_2 nanocubes. In Figure 1e, the interface relationship is Au(111) $[1\bar{2}1]$//CeO_2(001) [100]. Figure 1f shows a different epitaxy of Au nanoparticles on the CeO_2 (100) surface. The interface relationship is Au(111) $[\bar{1}10]$//CeO_2(001) [100]. For 50 particles analyzed, approximately 20% of them were Au(111) $[1\bar{2}1]$//CeO_2(001) [100] and the other 80% Au(111) $[\bar{1}10]$//CeO_2(001) [100]. In both cases, the first Au atomic layers at the Au-CeO_2 interface show an extra-bright contrast, which is attributed to the extended Au atomic layers, as illustrated in Figure 1h. Because of the extended layer feature, the growth of Au on CeO_2 nanocubes before the WGS reaction can be categorized as Stranski–Krastanov (SK) growth. The SK, Frank-Van der Merwe (FM), and Volmer-Weber (VW) growth modes are the three primary thin film growth modes, classified on the basis of interface thermodynamics.[47] Thus the extended layer will be referred to as the SK layer.

Figure 2a shows a HAADF image of a typical Au-CeO_2 nanorod after the WGS reaction. Only Au particles can be seen in all HAADF images, and the rafts have vanished after the reaction. The size (width) of 144 randomly selected Au nanoparticles supported by CeO_2 nanorods was measured before and after the WGS reaction (see the histograms of size distribution in the Supporting Information). The average size of the Au particles was ~5.0±1.5 nm both before and after the reaction, meaning the size remained constant during the WGS process. The general shape of the Au particle is illustrated in Figure 2b, which is similar to the Au particle shape on the nanorods before the WGS reaction (as illustrated in Figures 1c,g). In addition, the interlayer spacing measurement at the Au-CeO_2(111) interface shows a ~3.1 Å spacing between the first Au-Ce interlayer, which is almost the same as the spacing before the reaction (see Supporting Information for more details). Thus both the exposed facets and the atomic interface structure of the Au particles on CeO_2 nanorods are maintained. This connects to the observation that there is no significant change of the Au particle size and shape on the CeO_2 nanorods before and after the WGS reaction.

Figure 2c shows an example of the Au-CeO_2 nanocubes after the WGS reaction. It can be seen that the SK layers vanished after the reaction. Moreover, the average particle size (width) of 144 randomly selected Au nanoparticles increased from ~3.0±1.0 nm to ~3.8±1.2 nm (see histograms of the size distribution in the Supporting Information). In addition, the Au nanoparticle shape is slightly different before and after the reaction. As indicated in Figure 2c, additional {111} facets are present near the Au-CeO_2 support.

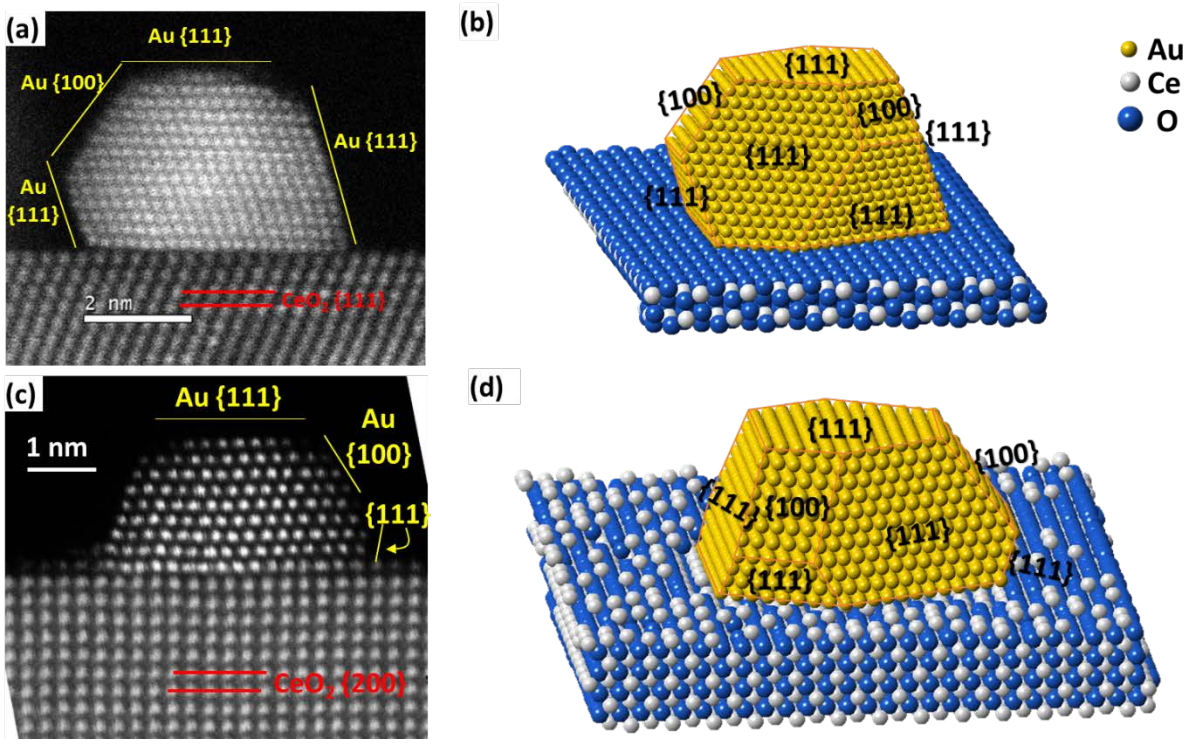

Figure 2. The morphology and atomic structures of Au-CeO_2 nanostructures after the WGS reaction (a) Atomic resolution HAADF image of an Au particle supported by a CeO_2 nanorod. (b) Schematic view of an Au particle supported by the CeO_2 (111) surface after the WGS reaction. (c) Atomic resolution HAADF image of an Au particle supported by a CeO_2 nanocube. (d) Atomic resolution HAADF image of an Au particle supported by the CeO_2 (100) surface after the WGS reaction.

According to the Wulff construction,[48] the shape of a free standing Au particle is shown in Figure 3a. For the particles grown on a substrate, the shape is truncated by the substrate. Assuming the height of a free standing particle is H and that of a particle grown on a substrate is h, as shown in Figure 3b, the truncation ratio (h/H) depends on the interface energy via the Winterbottom construction[48] and the truncation ratio increases as the interface energy increases. The truncation ratio of the Au particles on CeO_2 nanocubes increases significantly from ~0.37±0.06 for the cube to ~0.68±0.11 after the WGS reaction, as shown in Figure 3d. In

contrast, the truncation ration of Au particles on CeO_2 rods is similar before and after the WGS reaction (~0.63±0.06 versus ~0.66±0.06), as shown in Figure 3f. The relationship between the interfacial free energy and the truncation ratio can be written as

$$h/H=(2\gamma_{\{111\}}+\gamma_{int})/2\gamma_{\{111\}} \quad (1)$$

where γ_{int} is the interface free energy and γ_{sur} is the surface free energy of the metal. It is worth noting that the interfacial energy is a relative term, and the comparison is only valid only when the definition is the same (see more details about the equation derivation in the Supporting Infromation). Taking 0.094 eV/Å^2 as the surface free energy of the Au (111) surface[49] the interfacial free energies are -0.12 eV/Å^2 for the Au-CeO_2 nanocubes and -0.070 eV/Å^2 for the Au-CeO_2 nanorods before the WGS reaction. After the WGS reaction, the interface energy between the Au-CeO_2 nanorods is ~ -0.064 eV/Å^2 and ~-0.060 eV/Å^2 for the Au-CeO_2 nanocubes. The interface energy change of the Au-CeO_2 nanocubes (~0.06 eV/Å^2) is much more significant than the one for Au-CeO_2 nanorods (~0.006 eV/Å^2). The latter one is almost negligible.

There are a few details observed in other studies also observed in this study. We noticed there are Au particles with twins present (see the images in the Supporting Information). In these cases, the shape of free standing Au particles can be approximated using the modified Wulff construction.[50] As the contribution of the free energy of the twin boundary is rather small compared to the surface free energy,[50] we ignored the energy contribution of the twins when calculating the adhesion of the Au particles. We note that bulk Au atoms are almost inert in the catalysis,[22] so the twins should contribute negligible amounts to the catalytic activities (a point we will return to later). As a second detail, the Au particles supported by the CeO_2 nanorods undergo back-and-forth rotations which can cause the Au particles to appear to deviate slightly

from the zone axis and epitaxial orientation (see Supporting Information). More detailed discussion can be found in ref [51]. As another detail, the atomic structure of Au(100) surface is constantly changing during the imaging, possibly assisted by the electron beam, while the shape does not change much (see Supporting Information). Similar phenomena have been observed many times before either in a conventional TEM[52] or an environmental TEM.[53] The surface reconstruction of the Au (100) surface is well known, and will not be discussed further here.

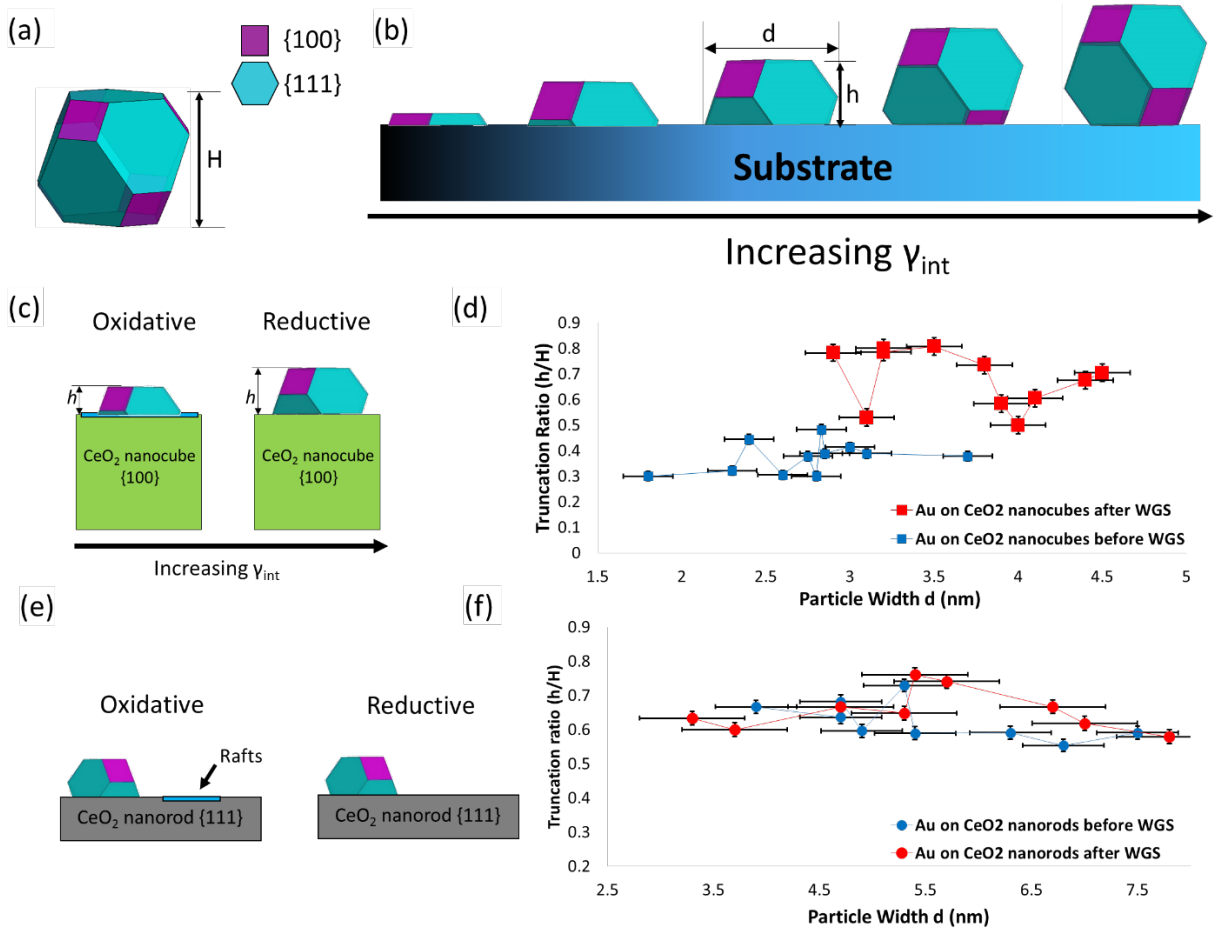

Figure 3. Illustration of the adhesion change of the Au-CeO_2 system under oxidative and reductive conditions. (a) Illustration of the Wulff construction of an Au particle. (b) The

Winterbottom construction of Au nanoparticles supported by substrates with different interface energies. The shapes of the Au particles after WGS reaction corresponds to the Winterbottom shape with increased interface energy. (c) Illustration of the change of adhesion between the Au particle and the CeO_2 nanocube under oxidative and reductive conditions, with the truncation ratio statics shown in (d). (e) Illustration of the change of adhesion between the Au particle and the CeO_2 nanorod under oxidative and reductive conditions, with the truncation ratio statistics shown in (f).

The results demonstrate substantial changes in the Au nanoparticle structure depending upon both whether they have been exposed to oxidative or reducing reaction conditions, and the orientation of the surface of the oxide support.

Consider first the (111) CeO_2 surfaces in the nanorods. According to Tasker's classification of oxide surfaces,[54] the O-terminated (111) surface is a stable non-polar surface while the Ce-terminated (111) surface is a polar surface. Thus there is a strong driving force to have an O-terminated (111) surface. It has been demonstrated experimentally that the CeO_2 (111) prefers to be O-terminated surface with few O vacancies,[17] and the oxide substrates were pre-annealed at 700 °C in air to reduce the number of surface defects. The interfacial free energy can be thought of as how easy it is for a surface to create new bonds, so on more stable surface the nanoparticle shape and adhesion should not change substantially, which is what we observed for Au on CeO_2 nanorods; for instance the interlayer spacing measurement shows a ~3.1Å spacing between the Au−Ce interlayer before and after the WGS reaction (see Supporting Information). The interlayer spacing is similar to the previously estimated spacing of the Au-CeO_2 interface with an O-terminated CeO_2(111) surface,[51, 55] which suggests that the same interface structure is

maintained. The only substantial change upon reduction is loss of the rafts which we attribute to atoms diffusing to the three-dimensional nanoparticles; the total number of atoms in the rafts was small so there was negligible change in the particle size. This is similar to a previous report that small Au clusters on the CeO_2 (111) surface migrates to larger particles in reductive conditions,[56] the exact reason for this is currently unknown. More details about the Au nucleation on the CeO_2 (111) surface was discussed in ref. 56.

The (100) CeO_2 surface behaves quite differently. According to Tasker's classification, CeO_2 (100) is a polar surface. Either Ce- or O-termination would lead to an unstable surface. Our previous study demonstrated that the (100) surface has several different surface terminations with a large number of Ce and O surface vacancies.[17] It has been reported that O vacancies at the O-terminated CeO_2 surfaces are preferential sites for the adsorption of Au atoms[57, 58], which is consistent with the stronger adhesion we observed. This also connects to the SK layer around the particles from conventional thin film growth thermodynamics. For the VW growth mode, the interactions between the metal adatoms are stronger than the metal-support interaction when misfit between the substrate and metal is included, thus 3D metal islands are formed. For the FM growth mode, the metal-support interaction is always stronger than the interactions between the metal adatoms, thus the metal grow in a layer-by-layer mode and wets the support. The SK growth is an intermediate growth process with competing energy terms from the metal-metal interactions including misfit strains and metal-support interaction. In this case the first Au monolayer metal-support interaction is stronger than the Au-Au interaction, but from the second layers onwards the Au-Au interaction is more important as is stress relief. Under reducing and reactive atmospheres, the strong metal-support interaction is lost and the Au particles switch to the VW mode. The weaker adhesion in the VW mode is consistent with the coarsening of the Au

particles. We note that the atomic surface structures of the CeO_2 (100) surface is similar to the surface before the reaction (see Supporting Information). Thus one implication is that the change in the interfacial energy upon reduction should be related to the presence of additional oxygen vacancies and Ce^{3+} at the Au-CeO_2 interfaces. The exact details of this would be a topic for future work.

The different behavior is qualitatively reflected in the catalytic activity. Figure 4 shows the percentage of CO conversion by the Au-CeO_2 nanocubes and nanorods during the WGS reaction as a function of time at 290 ºC. A significant decrease of the CO conversion is observed over time. At the later stages of the reaction, the catalysts stabilize with a lower CO conversion. Deactivation of Au/CeO_2 catalysts for the WGS reaction is commonly observed and has been mostly attributed to carbonates buildup and/or structural changes of the Au particles.[59] To better understand the role of carbonate species in the deactivation, temperature programmed desorption (TPD) was carried out on the two catalysts after the 40-hour WGS test. The CO_2-TPD profiles (See Supporting Information) showed that over 90% of the carbonate species desorb at the reaction temperature of 290 °C. A regeneration experiment was performed by purging the catalyst with He for 1 h in the middle of WGS reaction at 290 °C and then running the WGS reaction again. The activity test showed that regeneration at 290 °C in He only partially restored the WGS activity (see Supporting Information), thus we conclude that the deactivation is not only related to carbonate buildup but is also due to the structural change of the Au sites, i.e., loss of low-coordinate Au species (rafts on the CeO_2 nanorods and SK layers on the CeO_2 nanocubes) induced by WGS reaction and coarsening. With the same loadings of Au in both systems, the average size of the Au particles on the nanorods is ~ 1.8 and 1.2 nm larger than on the nanocubes before and after WGS reaction, respectively. Assuming that all Au atoms are in

the nanoparticles after the WGS reaction and Au-CeO_2 nanorods show higher activity throughout the reaction test, there are 1.7 times as many as the perimeter Au atoms (proportional to $1/d^2$, d is the diameter of Au particles[60]) for the CeO_2 nanocubes compared to those on the nanorods. It appears that the Au-CeO_2 nanorods are generally more active than the Au-CeO_2 nanocubes for the WGS reaction, consistent with the recent study[20] of WGS reaction over Au-CeO_2 nanostructures.

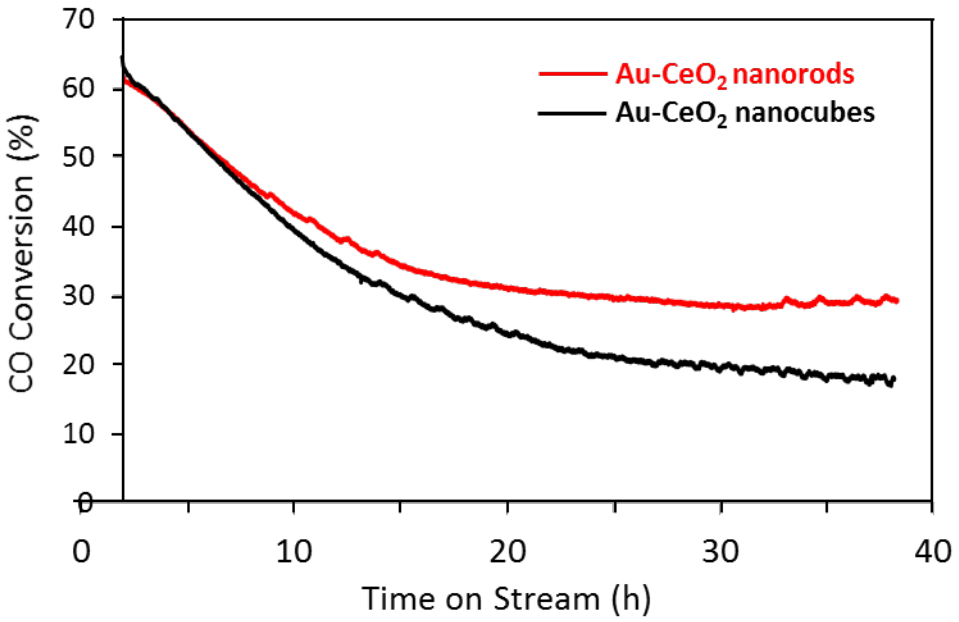

Figure 4. The CO conversion of Au-CeO_2 nanocubes and nanorods in the WGS reaction as a function as time at 290 ºC.

In summary, the oxidation state of the substrate plays a major role for both Au-CeO_2 systems, with larger adhesion for Au under oxidative condition. Under oxidative condition, Au particles with SK layers are present on the Au-CeO_2 nanocubes. The SK layers vanish and there is a morphological change of the Au particles after the WGS reaction, which is attributed to

reduction of the Au-CeO_2 (100) interface. In contrast, the Au-CeO_2 nanorods contain regular Au particles and some rafts under oxidative conditions. After the WGS reaction, the Au atoms in the rafts migrate to the particles. The Au particles on the CeO_2 nanorods are almost uncharged before and after the WGS reaction. The loss of strong adhesion of Au to the support CeO_2 (the SK layer and the rafts) is partly responsible for the decrease of the activities in the WGS reaction.

ASSOCIATED CONTENT

Supporting Information. Histograms of size distribution, atomic surface structures of CeO_2 (100) surface after the WGS reaction, Au particle back-and-forth rotation, Au(100) surface reconstructions, Au-CeO_2 interface spacing measurement, catalyst regeneration experiment, and the derivation of interface energy equation. This material is available free of charge via the Internet at http://pubs.acs.org.

Corresponding Authors

* Email: YuyuanLin2014@u.northwestern.edu (Y.L.); wuz1@ornl.gov (ZW)

l-marks@northwestern.edu (L.D.M.)

ACKNOWLEDGMENT

We acknowledge funding from Northwestern University Institute for Catalysis in Energy Processes (ICEP) on grant number DOE DE-FG02-03-ER15457 (Y.L., K.R.P. and L.D.M.). The STEM work was performed at the Research Sources Center at University of Illinois at Chicago. The HRTEM work was performed at Center for Nanoscale Materials at Argonne National Laboratory, a U.S. Department of Energy Office of Science Laboratory operated under Contract No. DE-AC02-06CH11357 by UChicago Argonne, LLC. Z.W. was supported by the U.S.

Department of Energy, Office of Science, Basic Energy Sciences, Chemical Sciences, Geosciences, and Biosciences Division. The catalytic test was conducted at the Center for Nanophase Materials Sciences, which is a DOE Office of Science User Facility. Y. Lin thanks Daniel Fowler and James A. McCarthy for very useful discussions.

REFERENCES

1. Polli, A. D.; Wagner, T.; Gemming, T.; Rühle, M. *Surf. Sci.* **2000,** 448, (2–3), 279-289.
2. Lin, Y.; Wen, J.; Hu, L.; Kennedy, R. M.; Stair, P. C.; Poeppelmeier, K. R.; Marks, L. D. *Phys. Rev. Lett.* **2013,** 111, (15), 156101.
3. Tauster, S. J. *Acc. Chem. Res.* **1987,** 20, (11), 389-394.
4. Tauster, S. J.; Fung, S. C. *J. Catal.* **1978,** 55, (1), 29-35.
5. Tauster, S. J.; Fung, S. C.; Baker, R. T. K.; Horsley, J. A. *Science* **1981,** 211, (4487), 1121-1125.
6. Tauster, S. J.; Fung, S. C.; Garten, R. L. *J. Am. Chem. Soc.* **1978,** 100, (1), 170-175.
7. Hayek, K.; Kramer, R.; Paál, Z. *Appl. Catal. A-Gen.* **1997,** 162, (1-2), 1-15.
8. Sadeghi, H. R.; Henrich, V. E. *J. Catal.* **1984,** 87, (1), 279-282.
9. Lin, X.; Nilius, N.; Freund, H. J.; Walter, M.; Frondelius, P.; Honkala, K.; Häkkinen, H. *Phys. Rev. Lett.* **2009,** 102, (20), 206801.
10. Lopez, N.; Janssens, T. V. W.; Clausen, B. S.; Xu, Y.; Mavrikakis, M.; Bligaard, T.; Nørskov, J. K. *J. Catal.* **2004,** 223, (1), 232-235.
11. Simoens, A. J.; Baker, R. T. K.; Dwyer, D. J.; Lund, C. R. F.; Madon, R. J. *J. Catal.* **1984,** 86, (2), 359-372.
12. Fu, Q.; Wagner, T. *Surf. Sci. Rep.* **2007,** 62, (11), 431-498.
13. Zhou, K.; Wang, X.; Sun, X.; Peng, Q.; Li, Y. *J. Catal.* **2005,** 229, (1), 206-212.
14. Yamada, Y.; Tsung, C.-K.; Huang, W.; Huo, Z.; Habas, S. E.; Soejima, T.; Aliaga, C. E.; Somorjai, G. A.; Yang, P. *Nat. Chem.* **2011,** 3, (5), 372-376.
15. Marks, L. D. *Rep. Prog. Phys.* **1994,** 57, (6), 603-649.
16. Sun, C.; Li, H.; Chen, L. *Energ. Environ. Sci.* **2012,** 5, (9), 8475-8505.
17. Lin, Y.; Wu, Z.; Wen, J.; Poeppelmeier, K. R.; Marks, L. D. *Nano Lett.* **2014,** 14, (1), 191-196.
18. Fu, Q.; Saltsburg, H.; Flytzani-Stephanopoulos, M. *Science* **2003,** 301, (5635), 935-938.
19. Kim, C. H.; Thompson, L. T. *J. Catal.* **2005,** 230, (1), 66-74.
20. Si, R.; Flytzani-Stephanopoulos, M. *Angew. Chem. Int. Ed.* **2008,** 47, (15), 2884-2887.
21. Lai, S.-Y.; Qiu, Y.; Wang, S. *J. Catal.* **2006,** 237, (2), 303-313.
22. Hammer, B.; Norskov, J. K. *Nature* **1995,** 376, (6537), 238-240.
23. Haruta, M.; Tsubota, S.; Kobayashi, T.; Kageyama, H.; Genet, M. J.; Delmon, B. *J. Catal.* **1993,** 144, (1), 175-192.
24. Chen, M. S.; Goodman, D. W. *Science* **2004,** 306, (5694), 252-255.
25. Liu, Y.; Jia, C.-J.; Yamasaki, J.; Terasaki, O.; Schüth, F. *Angew. Chem. Int. Ed.* **2010,** 49, (33), 5771-5775.
26. Yoon, B.; Häkkinen, H.; Landman, U. *J. Phys. Chem. A* **2003,** 107, (20), 4066-4071.
27. Guzman, J.; Gates, B. C. *J. Am. Chem. Soc.* **2004,** 126, (9), 2672-2673.
28. Mavrikakis, M.; Stoltze, P.; Nørskov, J. K. *Catal. Lett.* **2000,** 64, (2-4), 101-106.
29. Lopez-Acevedo, O.; Kacprzak, K. A.; Akola, J.; Häkkinen, H. *Nat. Chem.* **2010,** 2, (4), 329-334.

30. Liu, X. Y.; Wang, A.; Zhang, T.; Mou, C.-Y. *Nano Today* **2013,** 8, (4), 403-416.
31. Fu, Q.; Weber, A.; Flytzani-Stephanopoulos, M. *Catal. Lett.* **2001,** 77, (1-3), 87-95.
32. Andreeva, D.; Idakiev, V.; Tabakova, T.; Ilieva, L.; Falaras, P.; Bourlinos, A.; Travlos, A. *Catal. Today* **2002,** 72, (1–2), 51-57.
33. Sakurai, H.; Akita, T.; Tsubota, S.; Kiuchi, M.; Haruta, M. *Appl. Catal. A-Gen.* **2005,** 291, (1–2), 179-187.
34. Carrettin, S.; Concepción, P.; Corma, A.; López Nieto, J. M.; Puntes, V. F. *Angew. Chem. Int. Ed.* **2004,** 43, (19), 2538-2540.
35. Guzman, J.; Carrettin, S.; Corma, A. *J. Am. Chem. Soc.* **2005,** 127, (10), 3286-3287.
36. Wu, Z.; Schwartz, V.; Li, M.; Rondinone, A. J.; Overbury, S. H. *J. Phys. Chem. L* **2012,** 3, (11), 1517-1522.
37. Boucher, M. B.; Goergen, S.; Yi, N.; Flytzani-Stephanopoulos, M. *PCCP* **2011,** 13, (7), 2517-2527.
38. Guan, Y.; Ligthart, D. A. J. M.; Pirgon-Galin, Ö.; Pieterse, J. Z.; van Santen, R.; Hensen, E. M. *Top. Catal.* **2011,** 54, (5-7), 424-438.
39. Ta, N.; Liu, J.; Chenna, S.; Crozier, P. A.; Li, Y.; Chen, A.; Shen, W. *J. Am. Chem. Soc.* **2012,** 134, (51), 20585-20588.
40. Liu, J. *ChemCatChem* **2011,** 3, (6), 934-948.
41. Enterkin, J. A.; Poeppelmeier, K. R.; Marks, L. D. *Nano Lett.* **2011,** 11, (3), 993-997.
42. Sivaramakrishnan, S.; Wen, J.; Scarpelli, M.; Pierce, B.; Zuo, J.-M. *Phys. Rev. B* **2010,** 82, (19), 195421.
43. Gao, W.; Sivaramakrishnan, S.; Wen, J.; Zuo, J.-M. *Nano Lett.* **2015,** 15, (4), 2548-2554.
44. Wu, Z.; Li, M.; Howe, J.; Meyer, H. M.; Overbury, S. H. *Langmuir* **2010,** 26, (21), 16595-16606.
45. Zanella, R.; Giorgio, S.; Henry, C. R.; Louis, C. *J. Phys. Chem. B* **2002,** 106, (31), 7634-7642.
46. Tao, R.; Romanenko, A.; Cooley, L. D.; Klie, R. F. *J. Appl. Phys.* **2013,** 114, (4), 044306.
47. Bauer, E., Phänomenologische Theorie der Kristallabscheidung an Oberflächen. I. In *Zeitschrift für Kristallographie*, 1958; Vol. 110, p 372.
48. Winterbottom, W. L. *Acta Metall.* **1967,** 15, (2), 303-310.
49. Tyson, W. R.; Miller, W. A. *Surf. Sci.* **1977,** 62, (1), 267-276.
50. Marks, L. D. *J. Cryst. Growth* **1983,** 61, (3), 556-566.
51. Kuwauchi, Y.; Takeda, S.; Yoshida, H.; Sun, K.; Haruta, M.; Kohno, H. *Nano Lett.* **2013,** 13, (7), 3073-3077.
52. Surrey, A.; Pohl, D.; Schultz, L.; Rellinghaus, B. *Nano Lett.* **2012,** 12, (12), 6071-6077.
53. Yoshida, H.; Kuwauchi, Y.; Jinschek, J. R.; Sun, K.; Tanaka, S.; Kohyama, M.; Shimada, S.; Haruta, M.; Takeda, S. *Science* **2012,** 335, (6066), 317-319.
54. Tasker, P. W. *J. Phys. C: Solid. State.* **1979,** 12, (22), 4977.
55. Akita, T.; Tanaka, S.; Tanaka, K.; Haruta, M.; Kohyama, M. *J. Mater. Sci.* **2011,** 46, (12), 4384-4391.
56. Lu, J. L.; Gao, H. J.; Shaikhutdinov, S.; Freund, H. J. *Catal. Lett.* **2007,** 114, (1-2), 8-16.
57. Zhang, C.; Michaelides, A.; King, D. A.; Jenkins, S. J. *J. Phys. Chem. C* **2009,** 113, (16), 6411-6417.
58. Pan, Y.; Nilius, N.; Freund, H.-J.; Paier, J.; Penschke, C.; Sauer, J. *Phys. Rev. Lett.* **2013,** 111, (20), 206101.
59. Tao, F.; Ma, Z. *PCCP* **2013,** 15, (37), 15260-15270.
60. Cargnello, M.; Doan-Nguyen, V. V. T.; Gordon, T. R.; Diaz, R. E.; Stach, E. A.; Gorte, R. J.; Fornasiero, P.; Murray, C. B. *Science* **2013,** 341, (6147), 771-773.